Comprehensive performance analysis of perovskite solar cells based on different crystalline structures of MAPbI 3

Link to publication record in Ulster University Research Portal

Document Version
Publisher's PDF, also known as Version of record

Check for
updates

Comprehensive performance analysis of perovskite solar cells based on different crystalline structures of MAPbI$_3$

Khaled Gamal[1,2] · Mohammed Gamal[1,3] · Ali Okaz[2] · Nader Shehata[1,2,4,5,6] · Ishac Kandas[1,2]

Abstract

Perovskite solar cells (PSCs) have shown high optical absorption and consequently provide high conversion efficiency with stable performance. In our work, CH$_3$NH$_3$PbI$_3$ (MAPbI$_3$) as an absorber layer is analyzed for different crystalline structures. Cubic, tetragonal, and orthorhombic phases of perovskite material are investigated to check the impact of the crystalline structure on the solar cell performance. Both density of states and band structure are studied using Quantum-ESPRESSO package depending on density functional theory. Then, all relevant parameters were employed in SCAPS software and comprehensive study was done for examining the effect of the crystalline structure of perovskite layer on the solar cell performance. In-depth, analyses were conducted to evaluate key parameters, including open circuit voltage (V$_{oc}$), short circuit current (I$_{sc}$), fill factor (FF), and power conversion efficiency (PCE) considering the variations of perovskite layer thickness and bulk defect densities. The obtained results indicate that cells with cubic MAPbI$_3$, which shows a notably higher bandgap of 1.7 eV and an enhanced optical absorption coefficient, especially in the higher wavelength range (around 10^5 cm^{-1}), show better performance for almost all three scenarios. Cubic MAPbI$_3$ cells achieve relatively higher peak efficiency of 26% when the absorber layer thickness is almost 900 nm. The investigation into absorber bulk defect densities reveals the critical role of defect levels in PSC performance. Adjusting defect levels from 10^{14} cm^{-3} to 10^{18} cm^{-3} results in deteriorating trends in V$_{oc}$, J$_{sc}$, FF, and PCE. J$_{sc}$ remains stable until a defect level of 10^{17} cm^{-3}, highlighting a threshold where defects begin to impact charge carrier generation and separation. Doping effect has been studied, PCE remains stable until a critical doping level of 10^{16} cm^{-3} after which it drops significantly which indicates that doping is cautioned against due to its adverse effects on material and carrier transport. This finding holds significant promise for experimental solar cell fabrication, as it suggests that cubic MAPbI$_3$'s superior bandgap and enhanced optical absorption could lead to more efficient and robust photovoltaic devices in real-world applications.

Keywords Perovskite · MAPbI$_3$ · DFT · Band structure · DOS · Absorption coefficient · Solar cell efficiency · SCAPS-1D

Extended author information available on the last page of the article

⚫ Springer

1 Introduction

Various solar photovoltaic systems have been developed to efficiently convert light into electricity such as perovskite solar cells (PSCs), organic photovoltaics (OPVs) (Jia et al. 2023; Li et al. 2023a), copper indium gallium selenide (CIGS) solar cells (Jošt et al. 2022; Shrivastav et al. 2023), silicon solar cells (Zhou et al. 2022; Yeo et al. 2022), CdTe solar cells (Jain et al. 2023; Jamarkattel et al. 2022), gallium arsenide (GaAs) solar cells (Papež et al. 2020; Yun et al. 2022), and quantum dot solar cells (QDSCs) (Rasal et al. 2022). The pivotal factors for widespread application of these photovoltaic devices include their efficiency, manufacturing cost, and stability. Among these, PSCs have garnered attention due to their high efficiency, easy manufacturing processes, and cost-effectiveness (Li et al. 2023b). PSCs have rapidly emerged as a highly promising avenue for research, showcasing a confirmed efficiency of 26.1% since their introduction in 2013. In comparison, OPVs, initiated in 2001, currently achieve an efficiency of 19.2%. PSCs, despite their relatively recent entry, have swiftly progressed to efficiencies comparable to long-established technologies such as CIGS solar cells 23.6%, silicon solar cells 26.1%, CdTe 22.4%, and GaAs solar cells 27.8%, all introduced in the seventies of the last century. Additionally, perovskite solar cells outpace the efficiency of QDSCs, a more recent entrant since 2010, exhibit an efficiency of 18.1% (Best research-cell efficiency chart | photovoltaic research. 2024). This rapid progression solidifies PSCs as a leading candidate for ongoing research, hinting at their potential to outshine established solar cell technologies in efficiency. These hybrid perovskite materials, possessing an octahedral crystalline structure with the general formula ABX_3. The notable performance is credited to the unique attributes of halide perovskites, including a tunable bandgap, relatively simple fabrication through low-temperature methods, and adequate absorption capability (Feng and Nan 2022; Nnochin et al. 2023). Moreover, larger-scale roll-to-roll manufacturing techniques have facilitated extensive production, significantly enhanced the cost-efficiency of flexible PSCs, and signaled a promising outlook in the market (Othman et al. 2022; Chandrasekhar et al. 2022).

Recent years have witnessed a focused exploration of perovskite materials' electronic and optical properties through first-principles calculations, particularly employing density functional theory (DFT) (Lindblad et al. 2014; Even et al. 2014). This computational approach serves as a valuable tool for investigating the electronic structure of semiconductors and gaining insights into materials suitable for solar cells. Key among these insights is the study of optical absorption spectra, providing critical information on the electronic properties of the material (Wolf et al. 2014). Zhu et al. (2014) have contributed significantly by utilizing the GW approach to adjust quasiparticle energies, enhancing the accuracy of DFT descriptions for orthorhombic and tetragonal $MAPbI_3$ perovskite materials. Their research focused on the absorption spectrum of these materials and the identification of potential defects affecting the performance of PSCs. A gap between the first two absorption peaks was observed, indicating the potential significance of defect absorption in these materials. While Ahmed et al. (2015) conducted a thorough investigation of the optical properties of cubic $MAPbI_3$ using GW-augmented DFT calculations, emphasizing the heightened optical conductivity close to the band gap and the system's responsiveness to low-energy vibrational modes. The authors conducted calculations of the infrared (IR) absorption spectrum, yielding valuable insights into the material's optical properties. The literature also delves into the advantageous feature of tunable bandgaps offered by PSCs (Ong et al. 2019). Ong et al. explored how the

orientation of the local structure of $(CH_3NH_3)^+$ ions impact this bandgap. Additionally, the bandgap is influenced by the distortion of the PbI_3 cage, a result of interactions between the inorganic framework and the molecules.

This study aims to build upon the existing body of literature by presenting an electronic and optical analysis of the $MAPbI_3$ perovskite layer. The focus is on different crystalline structures, including cubic, tetragonal, and orthorhombic phases. The electronic structure will be analyzed by examining the density of states and band structure using the Quantum-ESPRESSO package (Giannozzi et al. 2009). Simultaneously, the optical spectrum will be obtained using DFT, and all relevant parameters will be applied in the SCAPS solar cell simulator, showcasing our commitment to go beyond DFT and comprehensively study the behavior of the solar cell. In addition to the electronic and optical analysis, this study will explore the I-V curve, fill factor, efficiency, V_{oc}, and I_{sc} as functions of the thickness of the perovskite layer. This multifaceted approach aims to provide comprehensive insights into the performance of perovskite solar cells and the optimum thickness of the perovskite layer for achieving maximum efficiency. In our work, the main goal is to establish clear connections between prior studies and the specific outcomes of this research. By delving into the electronic and optical properties of $MAPbI_3$ perovskite layers with different crystalline structures, this study contributes to a more nuanced understanding of the factors influencing the efficiency of perovskite solar cells.

The paper is structured as follows: Sec. 2 provides a detailed description of the computational methodology employed for DFT calculations and cell simulations using SCAPS. In Sec. 3, we present the results and engage in discussions concerning the influence of various $MAPbI_3$ structures, absorber thickness, dopant concentration, and defect density. Finally, in Sec. 4, we summarize our findings, draw conclusions, and outline potential directions for further research.

2 Computational methodology

Advancing the understanding of perovskite solar cells PSCs, our research uniquely explores $CH_3NH_3PbI_3$ ($MAPbI_3$) absorber layers with varied crystalline structures—cubic, tetragonal, and orthorhombic. Setting itself apart from prior studies, our approach involves a dual analytical method, integrating density functional theory (DFT) calculations (for density of states, band structure, and absorption coefficient) with the Quantum-ESPRESSO and YAMBO packages. The subsequent incorporation of these insights into SCAPS-1D software enables a comprehensive assessment of crucial parameters, including open circuit voltage (V_{oc}), short circuit current (I_{sc}), fill factor (FF), and power conversion efficiency (PCE). Importantly, our investigation delves into the impact of perovskite layer thickness, bulk defect densities and doping concentration on solar cell performance, offering a nuanced perspective.

2.1 DFT analysis

DFT calculations were performed using QuantumEspresso package (Giannozzi et al. 2009), which is a widely used software package for first-principles electronic structure calculations and materials modeling based on density functional theory. To analyze the electronic and optical properties of the $MAPbI_3$ perovskite layer, we utilized three different crystalline structures including cubic, tetragonal, and orthorhombic structures.

For the cubic structure, we used a MAPbI$_3$ unit cell with a Pm3m space group, which contained 12 atoms. In the tetragonal structure, we employed a MAPbI$_3$ unit cell with a P4/mmm space group, consisting of 48 atoms. Similarly, for the orthorhombic structure, we utilized a MAPbI$_3$ unit cell with a Pnma space group, also consisting of 48 atoms. Spin–orbit coupling (SOC) was not considered in the calculations. Unlike the common issue of bandgap underestimation, the calculated bandgaps using the generalized gradient approximation (GGA) and local density approximation (LDA) were found to be very similar to the experimental values (Mosconi et al. 2013; Chang et al. 2004). This unexpected agreement is a result of error cancellation, specifically the omission of the spin–orbit interaction leading to an overestimation of the band gap, which compensates for the underestimation error in the LDA/GGA calculation (Even et al. 2013).

In our system, we employed the SSSP (Standard Solid State Pseudopotentials) with precision pseudopotentials (Prandini et al. 2018) to describe the electron–ion interactions. These pseudopotentials were utilized in various calculations, such as self-consistent field (SCF), non-self-consistent field (NSCF), and band calculations. From these calculations, we obtained the density of states and band structure of the system. For the absorption calculations, we utilized dojo pseudopotentials for both the SCF and NSCF calculations (Setten et al. 2018). These potentials were specifically employed to capture the absorption properties of the system. The output files generated from these calculations, including the electronic structure information, were then passed to the YAMBO package (Sangalli et al. 2019; Marini et al. 2009). YAMBO was used for further analysis and processing of the absorption data. The YAMBO code is used to study the complex dielectric function in these MAPbI$_3$ structures. To do this, we need the initial electronic structure data from the ground state, which comes from density functional theory codes (Sangalli et al. 2019). In this study, we got this data using the Quantum Espresso Package. It is worth noting that the selection of pseudopotentials, calculation methods, and software packages can vary depending on the specific requirements of the study and the nature of the system being investigated. In our analysis, the SSSP with precision pseudopotentials, dojo pseudopotentials, and YAMBO code were chosen as the tools to model and analyze the electron–ion interactions and absorption properties of the system. The criteria of convergence for energy and forces were set to 10^{-5} atomic units. For the cubic structure, a $10 \times 10 \times 10$ k-point mesh was used to sample the Brillouin zone. For the tetragonal structure, a $6 \times 6 \times 4$ k-point mesh was utilized, while for the orthorhombic structure, a $6 \times 4 \times 6$ k-point mesh was used. The choice of k-point mesh is a compromise between computations analysis time and accuracy, we tested denser grids but observed subtle differences in convergence. The wave-function cut-off used was 47 Ry, and the charge density cut-off used was 424 Ry.

In the described computational process, "Ry" refers to Rydberg, a unit of energy commonly used in quantum mechanical calculations. The "wave-function cut-off" is a parameter that defines the maximum kinetic energy of the electrons included in the quantum mechanical calculations. Similarly, the "density cut-off" defines the highest allowed electron density in the calculations. These parameters are crucial in determining the precision and efficiency of the calculations.

The interaction between photons and electrons, from a quantum mechanical standpoint, involves absorption or emission of photons causing transitions between filled and unfilled states within the system (Bano et al. 2017). This process is explained through the concept of time dependent perturbations acting on the system's ground electronic state. To examine the optical response of the system, the frequency dependent dielectric

function, represented by the following Equation (Liu et al. 2021; Syah et al. 2021), is utilized:

$$\varepsilon(\omega) = 1 + \frac{8\pi}{\Omega N_k} \sum_{k,v,c} \frac{\left|\langle\phi_{kv}|\hat{v}|\phi_{kc}\rangle\right|^2}{\left(E_{kc} - E_{kv}\right)^2 \left(E_{kc} - E_{kv} - \omega - i\eta\right)} \tag{1}$$

where the cell volume is Ω, the total number of k-points in the Brillouin zone is N_k the operator of velocity is $\hat{v}$, ω is the angular frequency, and the opportune broadening factor is η. The occupied and unoccupied states are represented by these indices v and c respectively. Then we can calculate the frequency-dependent absorption coefficient, $\alpha(\omega)$ using the next formula (Liu et al. 2021; Syah et al. 2021):

$$\alpha(\omega) = \omega \sqrt{\frac{-Re[\varepsilon(\omega)] + \sqrt{Re[\varepsilon(\omega)]^2 + Im[\varepsilon(\omega)]^2}}{2}} \tag{2}$$

2.2 Solar cell modeling and simulation

The analysis and modeling of the device were carried out using SCAPS software (Burgelman et al. 2000). By solving the continuity equations for electrons and holes (Eqs. 3 and 4) along with Poisson equation (Eq. 5) (Almosni et al. 2017), the performance attributes of the device can be calculated as follows:

$$\frac{dn_p}{dt} = G_n - \frac{n_p - n_{p0}}{\tau_n} + n_p\mu_n\frac{d\xi}{dx} + \mu_n\xi\frac{dn_p}{dx} + D_n\frac{d^2n_p}{dx^2} \tag{3}$$

$$\frac{dp_n}{dt} = G_p - \frac{p_n - p_{n0}}{\tau_p} + p_n\mu_p\frac{d\xi}{dx} + \mu_p\xi\frac{dp_n}{dx} + D_p\frac{d^2p_n}{dx^2} \tag{4}$$

$$\frac{d}{dx}\left(-\in(x)\frac{d\psi}{dx}\right) = q\left[p(x) - n(x) + N_D^+(x) - N_A^-(x) + p_t(x) - n_t(x)\right] \tag{5}$$

The afore mentioned Eqs. (3–5) involve several variables and parameters. The symbol G represents the generation rate, while x corresponds to the direction along the thickness. The lifetimes of electrons and holes are expressed as τ_n and τ_p, respectively. The diffusion coefficient is represented by D, and q is the electron charge of and holes, respectively. ξ is used to indicate the electric field, and ψ represents the electro-static potential. Additionally, $N_A^-(x)$ and $N_D^+(x)$ represent the ionized acceptor and donor concentrations, while $n(x)$, $n_t(x)$, $p(x)$, and $p_t(x)$ represent the concentrations of free electrons, trapped electrons, free holes, and trapped holes, respectively.

The applied schematic diagram of solar cell is depicted in Fig. 1, which has been chosen due to its favorable attributes. These include its suitability for processing at temperatures below 150°°C, its capacity to minimize hysteresis effects, and its enhanced capability for the collection of charge carriers (Rahman et al. 2019). It illustrates the standard p-i-n structure of a perovskite solar cell fabricated on a glass substrate coated with ITO/FTO. The perovskite layer, $CH_3NH_3PbI_3$ (MAPbI_3), is situated between the hole transport material

Fig. 1 PSC structure used in the simulation
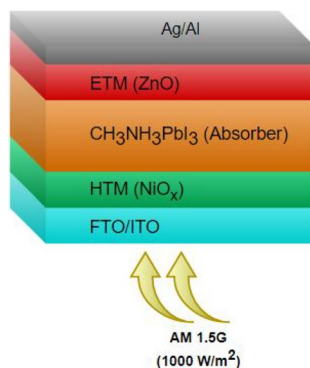
(HTM) and electron transport material (ETM) layers, with ZnO being utilized as the ETM and NiOx is employed as the HTM for all structures. ITO/FTO functions as the front-side contact, while Ag/Al serves as the back-side contact for the solar cell.

In our simulation, we initially focused on the study of different perovskite phases as absorber layer in the SCAPS package after obtaining the absorption spectrum from DFT calculations. In addition to the common cubic phase, we extended our investigation to include the tetragonal and orthorhombic phases too. By comparing the performance of the three different absorbers, we aimed to assess their respective efficiencies of perovskite solar cell and make meaningful comparisons.

3 Results and discussion

We have organized our computations and outcomes into two distinct categories. Firstly, we report the results obtained from DFT calculations for the electronic and optical properties of the $MAPbI_3$ perovskite in the three introduced crystalline structures. These calculations provide insights into the structural stability and electronic band structure of the $MAPbI_3$ perovskite in each of these phases. In the second part, we perform cell simulations using the SCAPS simulator. We consider the cubic, tetragonal, and orthorhombic structures of the $MAPbI_3$ perovskite as absorber layers in the solar cell simulation. The optical absorption spectra used in the simulation are obtained from the DFT calculations performed for each crystal structure. By utilizing different absorber structures and corresponding absorption spectra, we can analyze and compare the performance of the solar cell in terms of efficiency, fill factor, V_{oc}, and I_{sc} for each structure.

3.1 DFT calculation outcomes

3.1.1 Density of states

To assess the electrical characteristics, we investigated the electronic density of states as depicted in Fig. 2 for the cubic, tetragonal, and orthorhombic configurations of $MAPbI_3$. Evident from their density of state profiles is the semiconductive nature of these structures, attributed to minimal energy interval within the density of states. Prominent peaks are
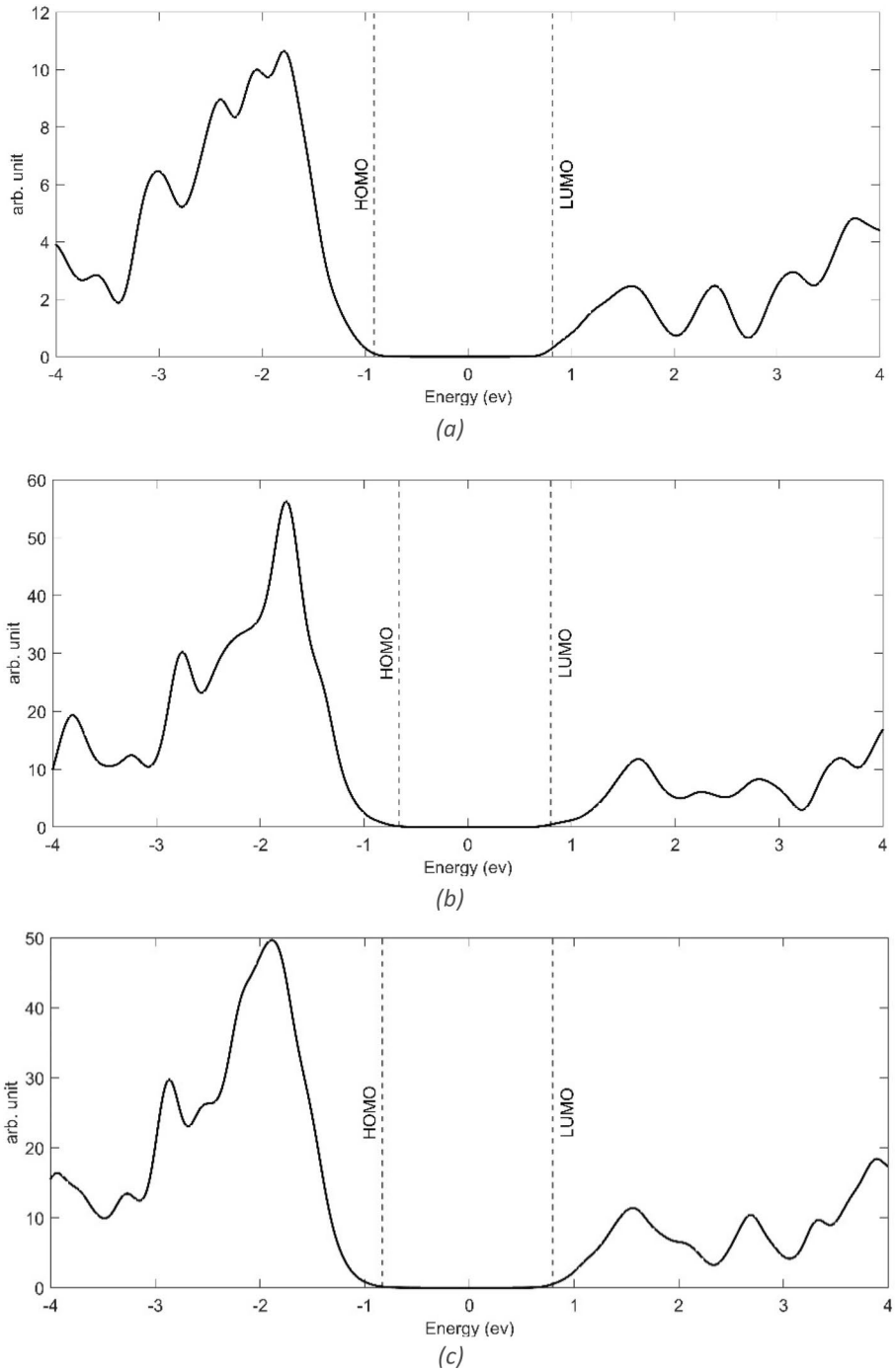
Fig. 2 Total density of states for three perovskite phases, **a** cubic, **b** tetragonal, and **c** orthorhombic

observable at approximately -1.8, -1.75, and -1.89 eV within the valence band, along with 3.73, 3.58, and 3.87 eV within the conduction band, spanning from -4 to 4 eV for the cubic, tetragonal, and orthorhombic arrangements, respectively. This pattern highlights distinct, well-defined peaks and substantial area coverage under the DOS curve, implying comparable electron accumulation across all three structures (Targhi et al. 2018).
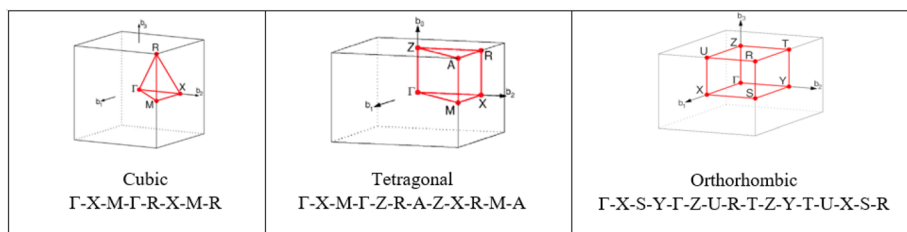
3.1.2 Band structure

For the computation of the band structures, we employed the lattice brillouin zone outlined in Fig. 3 (Setyawan and Curtarolo 2010). Then, the band structure of the different phases was analyzed. This analysis is important to understand some more properties such as carrier mobility and absorption spectrum (Jeng et al. 2013). As illustrated in Fig. 4 of the electronic band structures of MAPbI$_3$, the band gap values, which indicate the energy difference between valence and conduction bands, are measured as 1.7 eV, 1.5 eV, and 1.62 eV for cubic, tetragonal, and orthorhombic MAPbI$_3$ structures, respectively. These findings also align well with the results of previous theoretical density of states (DOS) calculations conducted in this study.

The analysis Indicates that the highest energy level of the valence band (VBM) and the lowest energy level of the conduction band (CBM) align at distinct points—the cubic structure at the R point and the tetragonal and orthorhombic structures at the Γ point, this is in good agreement with findings from a prior research by Lekesi et al. (2022). This alignment underscores their common classification as direct bandgap semiconductors.

### 3.1.3 Dielectric constants and absorption coefficients

In Fig. 5a, the real part of the dielectric function is shown, which tells us about how the material interacts with electric fields. Figure 5b, on the other hand, shows the imaginary part of the dielectric function, giving us more insight into the material's absorption behavior. The behavior of the imaginary part of the dielectric constant, directly linked to the material's absorption shown in Fig. 6, its maximum values, detected between 2 eV and 3.5 eV, correspond to wavelengths approximately from 350 to 650 nm—coinciding with the range where the absorption coefficient indicates significant values (Shaikh et al. 2016). The maximum absorption peaks for the cubic, tetragonal, orthorhombic crystalline structures are about 2.67, 3.06, and 3.15 eV respectively. However, the best absorption amplitude for the cubic structure is due to its high crystallinity (Bonadio et al. 2021). These peak shifts could be explained by Fig. 6 using the contrast between the band structure and DOS
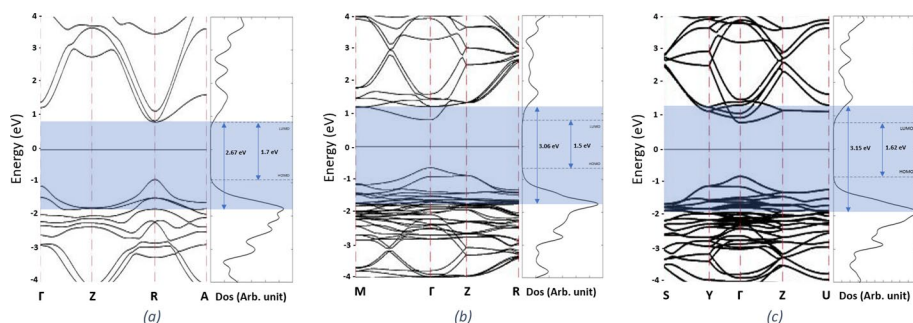

Cubic	Tetragonal	Orthorhombic
Γ-X-M-Γ-R-X-M-R	Γ-X-M-Γ-Z-R-A-Z-X-R-M-A	Γ-X-S-Y-Γ-Z-U-R-T-Z-Y-T-U-X-S-R

Fig. 3 Lattice brillouin zone for each structure

(a)

(b)

(c)
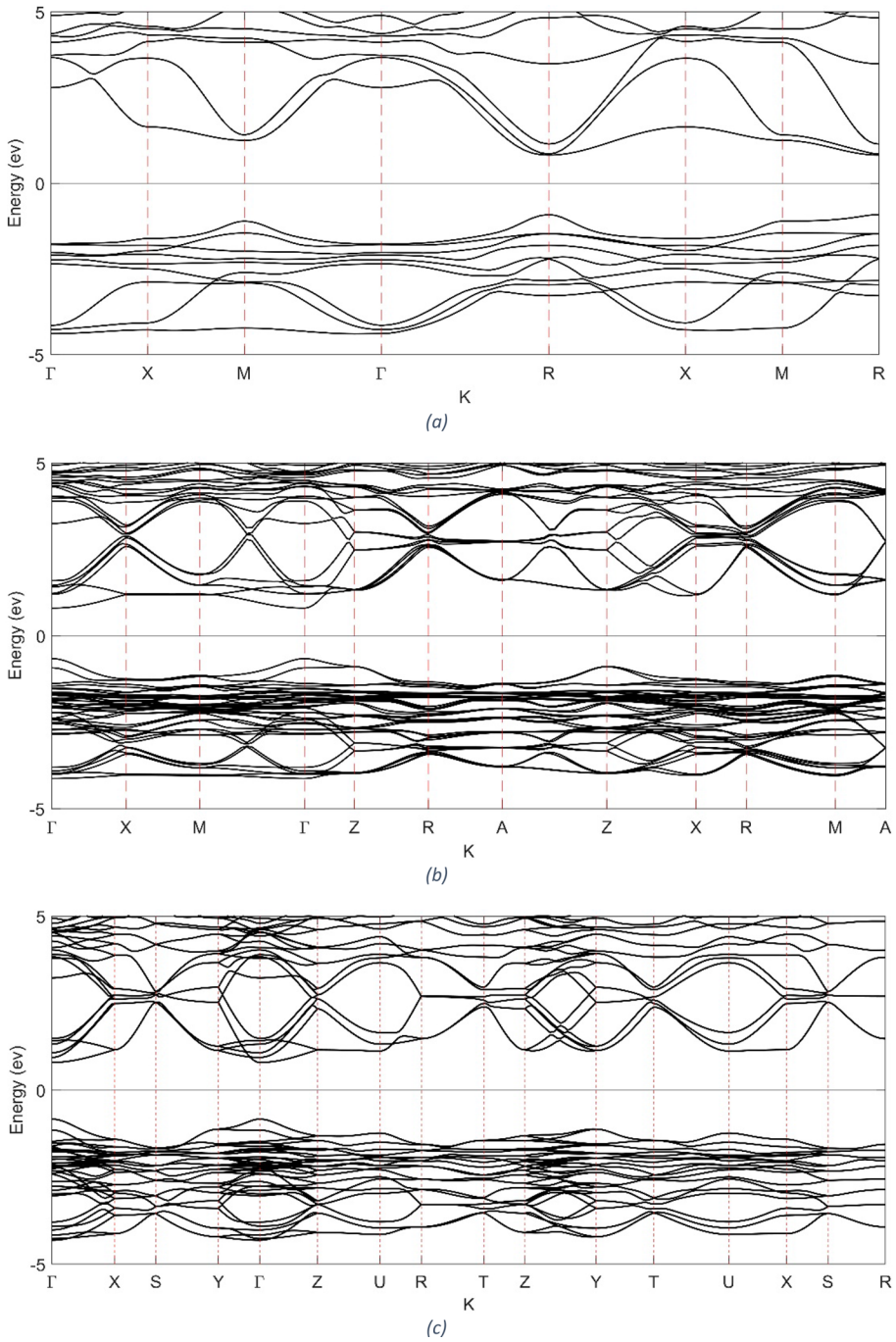
Fig. 4 Band structure for three perovskite phases, **a** cubic, **b** tetragonal, and **c** orthorhombic
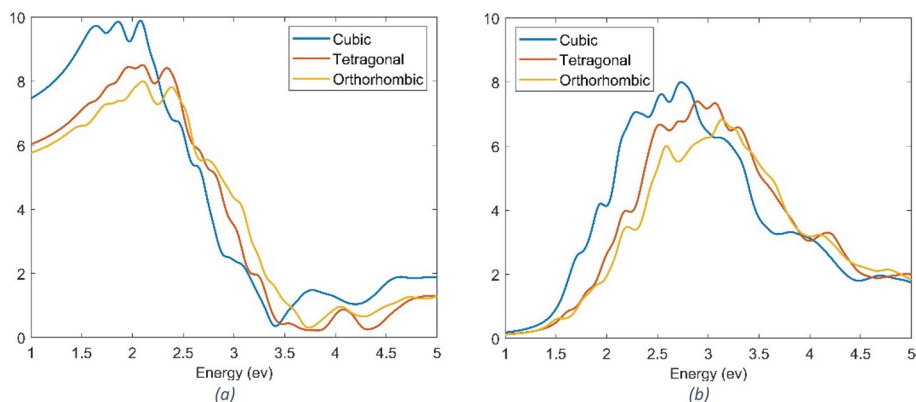
Fig. 5 Dielectric constant of MAPbI$_3$ structures. **a** Real part and **b** Imaginary part


Fig. 6 The contrast between the bandgap and the possible electron transition. **a** cubic, **b** tetragonal, and **c** orthorhombic phases

curves taking into consideration the possible transition according to the electron's population through the available energy levels as shown in Fig. 6.

The qualitative analysis of the graphs explains how the material responds to electric fields at that energy level. Moreover, the graphs highlight peaks, representing significant points where the material undergoes direct transitions when interacting with light. This detail is important for applications like solar cells and electronic devices (Hajjiah et al. 2022). Even though our analysis gives us a solid understanding, considering effects like phonons—vibrations in the material's lattice—might lead to small changes in the absorption coefficient (Liu et al. 2021).

Figure 7 compares the absorption coefficient obtained by YAMBO code for the three structures on the left axis, along with the solar irradiance (Mass and 1.5 Spectra.2024) on the right axis. The absorption coefficient curve exhibits elevated values within the low wavelength range, spanning from 300 to 900 nm, indicating pronounced light absorption in this interval. Conversely, the curve displays diminished absorption for longer wavelengths, underscoring a reduced tendency of the material to absorb light at lower energy levels. The absorption coefficient starts to increase at approximately 700 to 800 nm which corresponds to bandgaps values measured in eV. This alignment underscores the correlation between the material's absorption behavior and its energy band gap, with the observed transition
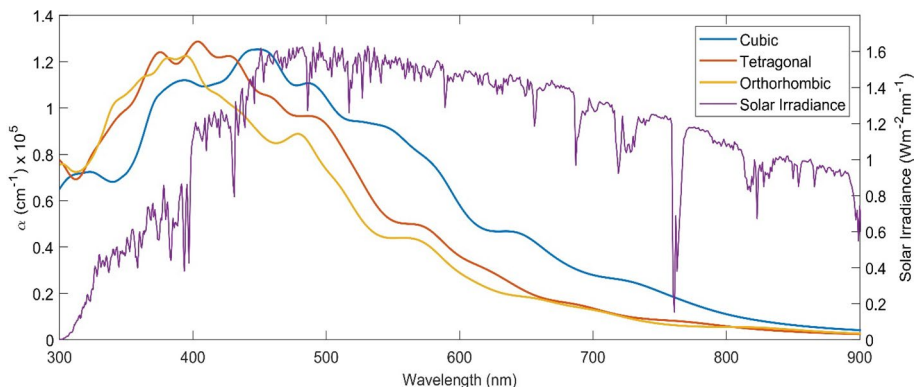
Fig. 7 MAPbI$_3$ structures' absorption spectrum

occurring within the range of the previously determined band gap energy levels. Notably, the cubic structure, specifically within the broader range from 450 to 900 nm, displays a higher absorption coefficient. This observation gains significance as it aligns with the wavelength range associated with high solar irradiance. The heightened absorption in this solar energy range suggests superior overall performance of the cubic structure compared to other configurations.

3.2 Solar cell simulation

All layers under investigation in this study are intrinsically undoped, implying the absence of external doping. However, due to the absence of a dedicated option for specifying carrier concentration within SCAPS, we employ acceptor concentration for p-type layers (NiO$_x$ and MAPbI$_3$), while for n-type layer (ZnO, the electron transport material), donor concentration is utilized. This adaptation is justified on the premise that dopants are treated as being completely ionized in the simulation (Rahman et al. 2019).

The perovskite material is regarded as marginally p-type, a characterization supported by multiple studies (Dong et al. 2015; Hutter et al. 2015). The selection of mobility for electrons and holes stems from thin film data (Herz 2017), as opposed to single crystal data, to accurately replicate the fabrication conditions. Mobility values are derived from Hall data and are distributed uniformly for both electrons and holes. This approach is grounded in the similarity of effective carrier masses in MAPbI$_3$, resulting in equal distribution of mobilities between the two carrier types (Leijtens et al. 2014). To ascertain the accuracy of our simulations, we conducted a comparison by simulating a MAPbI$_3$ solar cell using the absorption spectrum derived from density functional theory (DFT). The solar cell simulation is executed with the parameters outlined in Tables 1 and 2.

3.2.1 Comparison study of different MAPbI$_3$ structures

The p-i-n perovskite solar cell (PSC) structure is investigated with three distinct MAPbI$_3$ absorber layer configurations: cubic, tetragonal, and orthorhombic structures. ZnO serves as the electron transport material (ETM) for these configurations, while NiO$_x$ is employed

Table 1 SCAPS electrical and optical parameters of different layers

Properties	NiO$_x$	MAPbI$_3$ (cubic)	MAPbI$_3$ (orthorhombic)	MAPbI$_3$ (tetragonal)	ZnO
Thickness (nm)	80	320	320	320	80
Bandgap (eV)	3.75 (Ratcliff et al. 2012)	1.7	1.62	1.5	3.6 (Noh et al. 2018)
Affinity (eV)	2.1 (Ratcliff et al. 2012)	3.9 (Jeng et al. 2013)	3.9 (Jeng et al. 2013)	3.9 (Jeng et al. 2013)	4.1 (Noh et al. 2018)
Dielectric permittivity	10.7	10	8	8.5	8.1
DOS$_{CB}$ (cm^{-3})	2.8×10^{19} (Rödl and Schleife 2014)	2.76×10^{18} (Giorgi et al. 2013)	2.76×10^{18} (Giorgi et al. 2013)	2.76×10^{18} (Giorgi et al. 2013)	4.5×10^{18} (Hossain et al. 2003)
DOS$_{VB}$ (cm^{-3})	1.8×10^{19} (Rödl and Schleife 2014)	3.9×10^{19} (Giorgi et al. 2013)	3.9×10^{19} (Giorgi et al. 2013)	3.9×10^{19} (Giorgi et al. 2013)	1×10^{18} (Hossain et al. 2003)
μ$_e$ (cm^2/V s)	12 (Shan et al. 2016)	15 (Herz 2017)	15 (Herz 2017)	15 (Herz 2017)	300 (Makino et al. 2005)
μ$_h$ (cm^2/V s)	25 (Shan et al. 2016)	15 (Herz 2017)	15 (Herz 2017)	15 (Herz 2017)	1 (Makino et al. 2005)
N$_A$ (cm^{-3})	10^{15}	10^{11} (Dong et al. 2015)	10^{11} (Dong et al. 2015)	10^{11} (Dong et al. 2015)	0
N$_D$ (cm^{-3})	0	0	0	0	10^{19} (Makino et al. 2005)

Table 2 Defects used in SCAPS of different layers

Defect property	NiO$_x$	MAPbI$_3$	ZnO
Type	Acceptor	Neutral	Donor
Total density (cm^{-3})	10^{17}	1.5×10^{16}	10^{17}
Electron diffusion length L$_n$ (nm)	180	510	280
Hole diffusion length L$_h$ (nm)	800	510	51

as the hole transport material (HTM). The analysis maintains consistent parameters across these configurations, including a uniform absorber layer thickness of 320 nm, consistent absorber bulk defect densities at 1.5×10^{16} cm^{-3}, and uniform interface recombination rates represented by S$_n$ and S$_p$ with values of 10^4 cm/s (Rahman et al. 2019).The corresponding current–voltage characteristics for the three distinct phases are depicted in Fig. 8, and the solar cell performance parameters are summarized in Table 3.

It is observed that cubic structure has superior performance over both tetragonal and orthorhombic structures. Among the three materials, cubic MAPbI$_3$ shows improved V$_{oc}$ (about 86 mV higher than orthorhombic), FF (1.07% higher than orthorhombic) and J$_{sc}$ (4.54 ma/cm^2 higher than tetragonal). The underlying cause for this behavior can be attributed to the notably higher bandgap of the cubic structure compared to the other configurations accompanied with its higher absorption especially in the longer wavelength range, which leads to the generation of greater proportion of carriers compared to tetragonal and orthorhombic absorbers (Laali et al. 2020).

Fig. 8 I-V curve of 320 nm MAPbI$_3$ PSC for three different structures
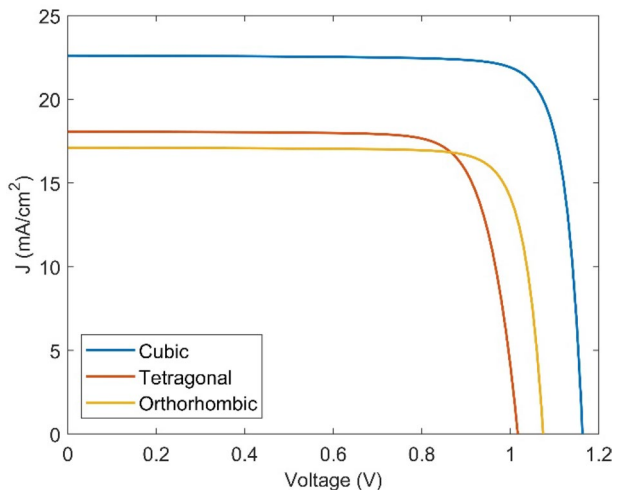
**Table 3** p-i-n perovskite solar cell performance parameters

Structure	V$_{oc}$ (V)	I$_{sc}$ (mA/cm^2)	FF (%)	PCE (%)
Cubic	1.16	22.6	84.17	22.13
Tetragonal	1.017	18.06	79.37	14.6
Orthorhombic	1.074	17.09	83.1	15.26

3.2.2 Absorber thickness variation

The thickness of the absorber layer should be chosen attentively to maximize the current density and not too large to minimize the reverse saturation current. To investigate the impact of the absorber (MAPbI$_3$) layer thickness on PSC performance, the thickness systematically varied from 300 to 1900 nm. This parameter variation is carried out while maintaining all other factors constant, including bulk defect densities, interface states, and other relevant parameters, for the three different structures. The outcomes of these investigations are illustrated in Fig. 9. The analysis reveals a consistent trend among all structures in response to the variation in thickness. With increasing thickness, both the open circuit voltage (V$_{oc}$) and fill factor (FF) exhibit a decline. The decrease in V$_{oc}$ as shown in Fig. 9a is attributed to the increment in the dark saturation current, which increases the recombination of the charge carriers (Ouslimane et al. 2021). That can be explained by the dependency of open-circuit voltage on the photo-generated current and dark saturation current, which is written as (Singh and Ravindra 2012):

$$V_{oc} = \frac{KT}{q} \ln \left[\frac{J_{sc}}{J_o} + 1 \right] \tag{6}$$

where $\frac{KT}{q}$ is the thermal voltage, J_{sc} is the photo-generated current density, and J_o is the saturation current density. While FF, Fig. 9b is inversely proportional to the thickness due
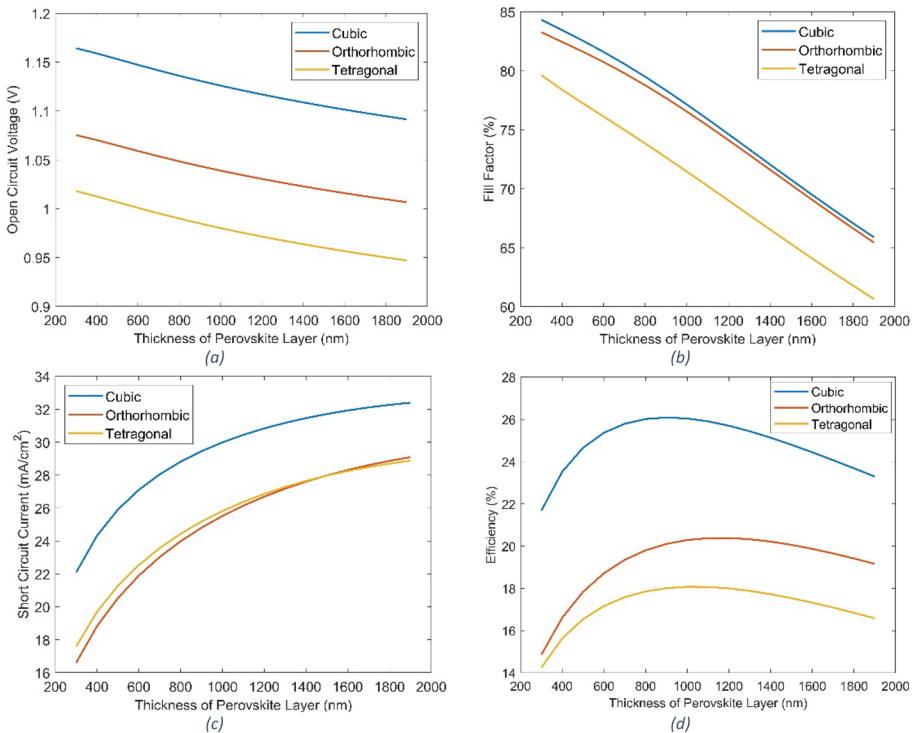
Fig. 9 Effect of thickness variation of MAPbI$_3$ layer on PSC performance

to an increased series resistance and an internal power dissipation in a thicker absorber layer.

Notably, an increase in absorber layer thickness leads to an incremented light absorption, resulting in a rise in the short circuit current density J_{sc}, Fig. 9c. As for the power conversion efficiency PCE, Fig. 9d, an optimal absorber thickness exists, beyond which the efficiency diminishes with further increases in thickness, this can be explained as thicker layers absorb more photons, generating more electron–hole pairs. Yet, as thickness increases further, recombination probability rises since charge carriers must travel longer distances for diffusion (Anwar et al. 2017). This behavior is found within all studied crystalline structures of perovskite. Among the examined structures, the cubic MAPbI$_3$ cells achieve an impressive efficiency peak of up to 26% at thickness 900 nm. In contrast, the tetragonal cells exhibit a maximum efficiency of approximately 18% at 1000 nm, while the cells incorporating orthorhombic MAPbI$_3$ material fall within the intermediate efficiency range of 20% at 1200 nm.
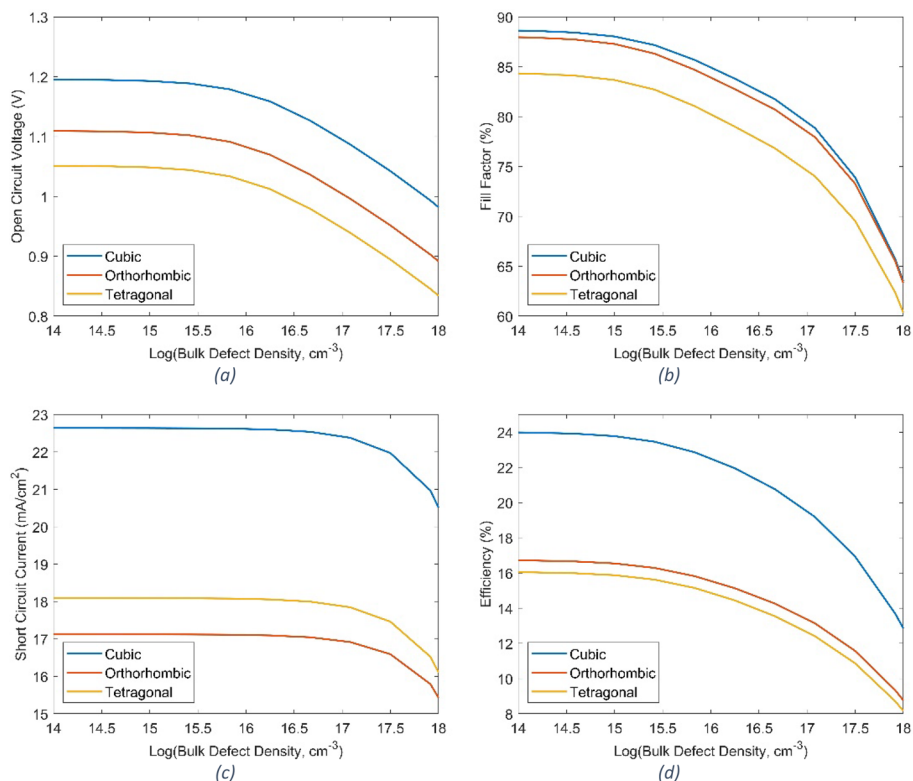
3.2.3 Absorber bulk defect densities

Perovskite materials exhibit distinctive characteristics such as extended carrier diffusion lengths, L_n for electrons and L_p for holes in single crystals. However, in thin films, these lengths can vary significantly based on the quality of the film. The diffusion length is intricately linked to the bulk defect densities within the perovskite (Rahman et al. 2019). To explore the impact of defect densities on the performance of perovskite solar cells (PSCs), the single bulk defect level is systematically adjusted across a range from 10^{14} cm^{-3} ($L_n = L_p = 6.2$ μm) to 10^{18} cm^{-3} ($L_n = L_p = 62$ nm). This alteration reflects the transition from a high-quality thin film perovskite layer to a layer of very poor quality. The results obtained from this analysis are summarized in Fig. 10a–d. As anticipated, each performance parameter V_{oc}, J_{sc}, FF, and PCE—exhibits a deteriorating trend with the introduced variation.

The bulk defect densities, N_{def}. are inversely proportional to the diffusion length as depicted in Table 4. So, in the case of low defects, diffusion length is in the order of micrometers while long diffusion lengths are indeed an important factor for highly efficient solar cells. In the other case of high defects, diffusion length is in the order of nanometers which reflects directly on the drop in solar cell efficiency, Fig. 10d (Akel et al. 2023). The FF is impacted by increasing defect density, Fig. 10b. This is because of the decreasing electric field with the increase of defect density which causes reduction in charge carrier. Hence, absorber layer quality is required for higher fill factor (Nalianya et al. 2021). The deterioration of V_{oc} in Fig. 10a can be explained by the reconfiguration of the band structure influenced by trap states which ultimately decreases the efficiency of solar cell (Raval et al. 2020).

However, an interesting exception arises in the case of current density, J_{sc}, as illustrated in Fig. 10c. Notably, J_{sc} remains stable until a defect level of 10^{17} cm^{-3} is reached, after which it commences a gradual decline. At low defect densities, this behavior can be attributed to the presence of defects that might not significantly impact the generation and separation of charge carriers. The short circuit current, Jsc, is primarily determined by the amount of photocurrent generated due to incident sunlight and the efficient separation of electron–hole pairs.

Fig. 10 Effect of bulk defect density variation of MAPbI$_3$ layer on PSC performance while keeping absorber thickness at 320 nm

Table 4 Defect density variation versus diffusion length

Defect density, $N_{def.}$ (cm^{-3})	1×10^{14}	1×10^{15}	1×10^{16}	1×10^{17}	1×10^{18}
Diffusion length, L (nm)	6200	2000	620	200	62

3.2.4 Absorber doping concentration

In this section, doping the active layer is studied and consequently its effect on the solar cell performance is presented. Here, we added acceptor material with concentration ranging from $N_A = 10^{14} cm^{-3}$ to $10^{18} cm^{-3}$. In Fig. 11, the variations of the different solar cell parameters are shown ending with the efficiency. It can be noted that, for all crystalline structures, the PCE is stable and begin to decrease significantly after $N_A \sim 10^{16} cm^{-3}$. However, the cubic structure still has the best performance ($PCE \sim 22\%$). This conclusion is consistent with Voc and J$_{sc}$ results shown in Fig. 11a, c respectively. That can be explained as the charge carriers are collected and transport easily below the threshold concentration $N_A \sim 10^{16} cm^{-3}$. For V_{oc} behavior, this can be attributed to an increase in Auger recombination with higher doping which in turn increases forward bias diffusion
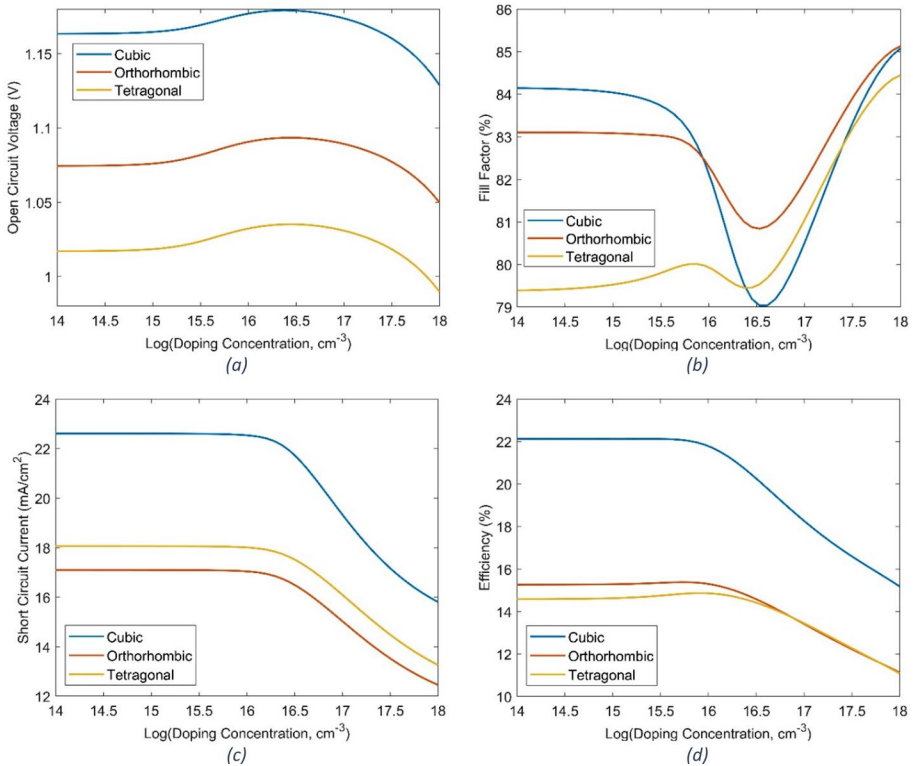
Fig. 11 Effect of doping concentration variation of MAPbI$_3$ layer on PSC performance while keeping absorber thickness at 320 nm

current hence reducing V_{oc} (Bertoluzzi et al. 2020). The fill factor, FF also is important parameter to be studied, Fig. 11b and almost have the same attitude except for higher doping concentrations. So, proper doping is required as heavy one lead to an increase in enhanced impurity scattering and Auger recombination rate and consequently, suppression of hole transportation (Minemoto and Murata 2014). Generally, excessive doping changes the nature of the perovskite material to be closer to metallic nature which impedes the carrier transport mechanisms (Stoumpos et al. 2013).

4 Conclusion

In this extensive study, we investigated the optical and electrical properties of MAPbI$_3$ with different crystalline structures to enhance solar cell performance. Using density functional theory (DFT) and QuantumEspresso, we explored density of states and band structures. Subsequently, the SCAPS software simulated perovskite solar cell performance. The cubic MAPbI$_3$ structure outshone tetragonal and orthorhombic structures, displaying higher V_{oc}, FF, and J_{sc}, primarily due to a higher bandgap and better light absorption. We also examined the impact of absorber layer thickness. Thicker layers improved J_{sc} but led to reduced V_{oc} and FF due to increased series resistance. An optimal thickness was found.

Among the structures, cubic *MAPbI*$_3$ achieved a peak efficiency of 26%, while tetragonal cells reached approximately 18%, and orthorhombic cells fell in between. We analyzed defect densities' influence on solar cell performance, revealing deteriorations in key parameters with increasing defects, especially when defect levels exceeded $10^{17} cm^{-3}$. The study on doping effects reveals that the PCE remains consistent until reaching a critical doping level of $10^{16} cm^{-3}$, beyond which a notable decrease is observed. This highlights the cautionary note against doping, emphasizing its adverse impact on both material and carrier transport. This research advances perovskite solar cell technology, emphasizing the potential of the cubic structure in the absorber layer for future exploration and development.

Supplementary Information The online version contains supplementary material available at https://doi.org/10.1007/s11082-024-06655-6.

Data availability Data and input files used in this simulation can be found in the supplementary document. Any additional data will be available upon request.

Declarations

Conflict of Interest The authors have no conflicts of interest to declare. All co-authors have seen and agree with the contents of the manuscript.

References

Ahmed, T., Salim, T., Lam, Y., Chia, E.E., Zhu, J.-X.: Optical properties of organometallic perovskite: an ab initio study using relativistic GW correction and Bethe-Salpeter equation. Europhys. Lett. **108**(6), 1–21 (2015)

Akel, S., Kulkarni, A., Rau, U., Kirchartz, T.: Relevance of long diffusion lengths for efficient halide perovskite solar cells. PRX Energy **2**(1), 013004 (2023)

Almosni, S., Cojocaru, L., Li, D., Uchida, S., Kubo, T., Segawa, H.: Tunneling-assisted trapping as one of the possible mechanisms for the origin of hysteresis in perovskite solar cells. Energ. Technol. **5**(10), 1767–1774 (2017)

Anwar, F., Mahbub, R., Satter, S.S., Ullah, S.M.: Effect of different HTM layers and electrical parameters on ZnO nanorod-based lead-free perovskite solar cell for high-efficiency performance. Int. J. Photoenergyphotoenergy (2017). https://doi.org/10.1155/2017/9846310

Bano, A., Khare, P., Gaur, N.: Electro-optic response of metal halide $CsPbI_3$ $CsPbI_3$: a first-principles study. Pramana **89**, 1–7 (2017)

Bertoluzzi, L., Boyd, C.C., Rolston, N., Xu, J., Prasanna, R., O'Regan, B.C., McGehee, M.D.: Mobile ion concentration measurement and open-access band diagram simulation platform for halide perovskite solar cells. Joule **4**(1), 109–127 (2020)

Best research-cell efficiency chart | photovoltaic research. NREL n.d. https://www.nrel.gov/pv/cell-efficiency.html. Accessed 30 Jan 2024

Bonadio, A., Escanhoela, C., Sabino, F., Sombrio, G., De Paula, V., Ferreira, F., Janotti, A., Dalpian, G., Souza, J.: Entropy-driven stabilization of the cubic phase of MaPbI 3 at room temperature. J. Mater. Chem. A **9**(2), 1089–1099 (2021)

Burgelman, M., Nollet, P., Degrave, S.: Modelling polycrystalline semiconductor solar cells. Thin Solid Films **361**, 527–532 (2000)

Chandrasekhar, P., Chapagain, S., Blake, M., Armstrong, P.J., Grapperhaus, C., Druffel, T.L.: Rapid scalable fabrication of roll-to-roll slot-die coated flexible perovskite solar cells using intense pulse light annealing. Sustain. Energy Fuels **6**(23), 5316–5323 (2022)

Chang, Y., Park, C.H., Matsuishi, K.: First-principles study of the Structural and the electronic properties of the lead-Halide-based inorganic-organic perovskites (CH~3NH~3) PbX~3 and CsPbX~3 (X=Cl, Br, I). J. Korean Phys. Soc. **44**, 889–893 (2004)

De Wolf, S., Holovsky, J., Moon, S.-J., Loper, P., Niesen, B., Ledinsky, M., Haug, F.-J., Yum, J.-H., Ballif, C.: Organometallic halide perovskites: sharp optical absorption edge and its relation to photovoltaic performance. J. Phys. Chem. Lett. **5**(6), 1035–1039 (2014)

Dong, Q., Fang, Y., Shao, Y., Mulligan, P., Qiu, J., Cao, L., Huang, J.: Electron-hole diffusion lengths> 175 μm in solution-grown $CH_3NH_3PbI_3$ single crystals. Science **347**(6225), 967–970 (2015)

Even, J., Pedesseau, L., Jancu, J.-M., Katan, C.: Importance of spin–orbit coupling in hybrid organic/inorganic perovskites for photovoltaic applications. J. Phys. Chem. Lett. **4**(17), 2999–3005 (2013)

Even, J., Pedesseau, L., Jancu, J.M., Katan, C.: DFT and kp modelling of the phase transitions of lead and tin halide perovskites for photovoltaic cells. Phys. Status Solidi Rapid Res. Lett. **8**(1), 31–35 (2014)

Feng, Q., Nan, G.: Crystalline phases regulate electronic trap states at defective surfaces of lead halide perovskites. J. Phys. Chem. Lett. **13**(49), 11473–11480 (2022)

Giannozzi, P., Baroni, S., Bonini, N., Calandra, M., Car, R., Cavazzoni, C., Ceresoli, D., Chiarotti, G.L., Cococcioni, M., Dabo, I.: QUANTUM ESPRESSO: a modular and open-source software project for quantum simulations of materials. J. Phys. Condens. Matter **21**(39), 395502 (2009)

Giorgi, G., Fujisawa, J.-I., Segawa, H., Yamashita, K.: Small photocarrier effective masses featuring ambipolar transport in methylammonium lead iodide perovskite: a density functional analysis. J. Phys. Chem. Lett. **4**(24), 4213–4216 (2013)

Hajjiah, A., Gamal, M., Kandas, I., Gorji, N.E., Shehata, N.: DFT and AMPS-1D simulation analysis of all-perovskite solar cells based on $CsPbI_3/FAPbI_3$ bilayer structure. Sol. Energy Mater. Sol. Cells **248**, 112026 (2022)

Herz, L.M.: Charge-carrier mobilities in metal halide perovskites: fundamental mechanisms and limits. ACS Energy Lett. **2**(7), 1539–1548 (2017)

Hossain, F.M., Nishii, J., Takagi, S., Ohtomo, A., Fukumura, T., Fujioka, H., Ohno, H., Koinuma, H., Kawasaki, M.: Modeling and simulation of polycrystalline ZnO thin-film transistors. J. Appl. Phys. **94**(12), 7768–7777 (2003)

Hutter, E.M., Eperon, G.E., Stranks, S.D., Savenije, T.J.: Charge carriers in planar and meso-structured organic–inorganic perovskites: mobilities, lifetimes, and concentrations of trap states. J. Phys. Chem. Lett. **6**(15), 3082–3090 (2015)

Jain, S.K., Sharma, G., Vyas, S.: Influence of hole interface layer on the performance of cadmium telluride-based thin film solar cell. Mater. Today Proc. **74**, 231–233 (2023)

Jamarkattel, M.K., Phillips, A.B., Subedi, I., Abudulimu, A., Bastola, E., Li, D.-B., Mathew, X., Yan, Y., Ellingson, R.J., Podraza, N.J.: Indium gallium oxide emitters for high-efficiency CdTe-based solar cells. ACS Appl. Energy Mater. **5**(5), 5484–5489 (2022)

Jeng, J.-Y., Chiang, Y.-F., Lee, M.-H., Peng, S.-R., Guo, T.-F., Chen, P., Wen, T.-C.: Methylammonium lead iodide perovskite/fullerene-based hybrid solar cells. SPIE Newsroom (2013). https://doi.org/10.1117/2.1201307.005033

Jia, Z., Ma, Q., Chen, Z., Meng, L., Jain, N., Angunawela, I., Qin, S., Kong, X., Li, X., Yang, Y.: Near-infrared absorbing acceptor with suppressed triplet exciton generation enabling high performance tandem organic solar cells. Nat. Commun. **14**(1), 1236 (2023)

Jošt, M., Köhnen, E., Al-Ashouri, A., Bertram, T., Tomšič, S., Magomedov, A., Kasparavicius, E., Kodalle, T., Lipovšek, B., Getautis, V.: Perovskite/CIGS tandem solar cells from certified 24.2% toward 30% and beyond. ACS Energy Lett. **7**(4), 1298–1307 (2022)

Laali, J., Hamedani, A., Alahyarizadeh, G., Minuchehr, A.: Performance analysis of the perovskite solar cells by a realistic, DFT-accurate optical absorption spectrum. Superlattices Microstruct. **143**, 106551 (2020)

Leijtens, T., Stranks, S.D., Eperon, G.E., Lindblad, R., Johansson, E.M., McPherson, I.J., Rensmo, H., Ball, J.M., Lee, M.M., Snaith, H.J.: Electronic properties of meso-superstructured and planar organometal halide perovskite films: charge trapping, photodoping, and carrier mobility. ACS Nano **8**(7), 7147–7155 (2014)

Lekesi, L.P., Koao, L.F., Motloung, S.V., Motaung, T.E., Malevu, T.: Developments on perovskite solar cells (PSCs): a critical review. Appl. Sci. **12**(2), 672 (2022)

Li, Y., Huang, X., Sheriff, H.K., Jr., Forrest, S.R.: Semitransparent organic photovoltaics for building-integrated photovoltaic applications. Nat. Rev. Mater. **8**(3), 186–201 (2023a)

Li, X., Yu, H., Liu, Z., Huang, J., Ma, X., Liu, Y., Sun, Q., Dai, L., Ahmad, S., Shen, Y.: Progress and challenges toward effective flexible perovskite solar cells. Nano-Micro Lett. **15**(1), 206 (2023b)

Lindblad, R., Bi, D., Park, B.-W., Oscarsson, J., Gorgoi, M., Siegbahn, H., Odelius, M., Johansson, E.M., Rensmo, H.K.: Electronic structure of $TiO_2/CH_3NH_3PbI_3$ perovskite solar cell interfaces. J. Phys. Chem. Lett. **5**(4), 648–653 (2014)

Liu, S., Wang, J., Hu, Z., Duan, Z., Zhang, H., Zhang, W., Guo, R., Xie, F.: Role of organic cation orientation in formamidine based perovskite materials. Sci. Rep. **11**(1), 20433 (2021)

Makino, T., Segawa, Y., Tsukazaki, A., Ohtomo, A., Kawasaki, M.: Electron transport in ZnO thin films. Appl. Phys. Lett. (2005). https://doi.org/10.1063/1.1991994

Marini, A., Hogan, C., Grüning, M., Varsano, D.: Yambo: an ab initio tool for excited state calculations. Comput. Phys. Commun. **180**(8), 1392–1403 (2009)

Minemoto, T., Murata, M.: Impact of work function of back contact of perovskite solar cells without hole transport material analyzed by device simulation. Curr. Appl. Phys. **14**(11), 1428–1433 (2014)

Mosconi, E., Amat, A., Nazeeruddin, M.K., Gratzel, M., De Angelis, F.: First-principles modeling of mixed halide organometal perovskites for photovoltaic applications. J. Phys. Chem. C **117**(27), 13902–13913 (2013)

Nalianya, M.A., Awino, C., Barasa, H., Odari, V., Gaitho, F., Omogo, B., Mageto, M.: Numerical study of lead free $CsSn_{0.5}Ge_{0.5}I_3$ perovskite solar cell by SCAPS-1D. Optik **248**, 168060 (2021)

Nnochin, S.C., Chibueze, T.C., Nkele, A.C., Ezugwu, S., Asogwa, P.U., Raji, A.T., Ekuma, C.E., Ezema, F.I.: Experimental and theoretical analysis of doping methylammonium lead iodide perovskite thin films with barium and magnesium. J. Mater. Sci. Mater. Electron. **34**(19), 1490 (2023)

Noh, M.F.M., Teh, C.H., Daik, R., Lim, E.L., Yap, C.C., Ibrahim, M.A., Ludin, N.A., bin Mohd Yusoff, A.R., Jang, J., Teridi, M.A.M.: The architecture of the electron transport layer for a perovskite solar cell. J. Mater. Chem. C **6**(4), 682–712 (2018)

Ong, K.P., Wu, S., Nguyen, T.H., Singh, D.J., Fan, Z., Sullivan, M.B., Dang, C.: Multi band gap electronic structure in $CH_3NH_3PbI_3$. Sci. Rep. **9**(1), 2144 (2019)

Othman, M., Zheng, F., Seeber, A., Chesman, A.S., Scully, A.D., Ghiggino, K.P., Gao, M., Etheridge, J., Angmo, D.: Millimeter-sized clusters of triple cation perovskite enables highly efficient and reproducible roll-to-roll fabricated inverted perovskite solar cells. Adv. Func. Mater. **32**(12), 2110700 (2022)

Ouslimane, T., Et-Taya, L., Elmaimouni, L., Benami, A.: Impact of absorber layer thickness, defect density, and operating temperature on the performance of MAPbI$_3$ solar cells based on ZnO electron transporting material. Heliyon **7**(3), e06379 (2021)

Papež, N., Gajdoš, A., Sobola, D., Dallaev, R., Macků, R., Škarvada, P., Grmela, L.: Effect of gamma radiation on properties and performance of GaAs based solar cells. Appl. Surf. Sci. **527**, 146766 (2020)

Prandini, G., Marrazzo, A., Castelli, I.E., Mounet, N., Marzari, N.: Precision and efficiency in solid-state pseudopotential calculations. NPJ Comput. Mater. **4**(1), 72 (2018)

Rahman, M.S., Miah, S., Marma, M.S.W., Sabrina, T.: Simulation based investigation of inverted planar perovskite solar cell with all metal oxide inorganic transport layers. In: 2019 International Conference on Electrical, Computer and Communication Engineering (ECCE), IEEE (2019)

Rasal, A.S., Yadav, S., Kashale, A.A., Altaee, A., Chang, J.-Y.: Stability of quantum dot-sensitized solar cells: a review and prospects. Nano Energy **94**, 106854 (2022)

Ratcliff, E.L., Meyer, J., Steirer, K.X., Armstrong, N.R., Olson, D., Kahn, A.: Energy level alignment in PCDTBT: PC70BM solar cells: solution processed NiOx for improved hole collection and efficiency. Org. Electron. **13**(5), 744–749 (2012)

Raval, D., Jani, M., Tripathi, B., Verma, D., Kumar, M.: Role of defect density on the electronic transport and current-voltage characteristics of the hole transporter free perovskite solar cell. Mater. Today: Proc. **28**, 223–229 (2020)

Reference Air Mass 1.5 Spectra. NREL n.d. https://www.nrel.gov/grid/solar-resource/spectra-am1.5.html. Accessed 30 Jan 2024

Rödl, C., Schleife, A.: Schleife, photoemission spectra and effective masses of n-and p-type oxide semiconductors from first principles: ZnO, CdO, SnO_2, MnO, and NiO. Phys. Status Solidi (a) **211**(1), 74–81 (2014)

Sangalli, D., Ferretti, A., Miranda, H., Attaccalite, C., Marri, I., Cannuccia, E., Melo, P., Marsili, M., Paleari, F., Marrazzo, A.: Many-body perturbation theory calculations using the yambo code. J. Phys. Condens. Matter. **31**(32), 325902 (2019)

Setyawan, W., Curtarolo, S.: High-throughput electronic band structure calculations: challenges and tools. Comput. Mater. Sci. **49**(2), 299–312 (2010)

Shaikh, P.A., Shi, D., Retamal, J.R.D., Sheikh, A.D., Haque, M.A., Kang, C.-F., He, J.-H., Bakr, O.M., Wu, T.: Schottky junctions on perovskite single crystals: light-modulated dielectric constant and self-biased photodetection. J. Mater. Chem. C **4**(35), 8304–8312 (2016)

Shan, F., Liu, A., Zhu, H., Kong, W., Liu, J., Shin, B., Fortunato, E., Martins, R., Liu, G.: High-mobility p-type NiOx thin-film transistors processed at low temperatures with Al_2O_3 high-k dielectric. J. Mater. Chem. C **4**(40), 9438–9444 (2016)

Shrivastav, N., Kashyap, S., Madan, J., Al-Mousoi, A.K., Mohammed, M.K., Hossain, M.K., Pandey, R., Ramanujam, J.: Perovskite-CIGS monolithic tandem solar cells with 297% efficiency: a numerical study. Energy Fuels **37**(4), 3083–3090 (2023)

Singh, P., Ravindra, N.M.: Temperature dependence of solar cell performance—an analysis. Sol. Energy Mater. Sol. Cells **101**, 36–45 (2012)

Stoumpos, C.C., Malliakas, C.D., Kanatzidis, M.G.: Semiconducting tin and lead iodide perovskites with organic cations: phase transitions, high mobilities, and near-infrared photoluminescent properties. Inorg. Chem. **52**(15), 9019–9038 (2013)

Syah, R., Davarpanah, A., Nasution, M.K., Wali, Q., Ramdan, D., Albaqami, M.D., Ouladsmane, M., Noori, S.M.: The effect of structural phase transitions on electronic and optical properties of $CsPbI_3$ pure inorganic perovskites. Coatings **11**(10), 1173 (2021)

Targhi, F.F., Jalili, Y.S., Kanjouri, F.: $MAPbI_3$ and $FAPbI_3$ perovskites as solar cells: case study on structural, electrical and optical properties. Results Phys. **10**, 616–627 (2018)

van Setten, M.J., Giantomassi, M., Bousquet, E., Verstraete, M.J., Hamann, D.R., Gonze, X., Rignanese, G.-M.: The PseudoDojo: training and grading a 85 element optimized norm-conserving pseudopotential table. Comput. Phys. Commun. **226**, 39–54 (2018)

Yeo, Z., Ling, Z., Ho, J., Lim, Q., So, Y., Wang, S.: Status review and future perspectives on mitigating light-induced degradation on silicon-based solar cells. Renew. Sustain. Energy Rev. **159**, 112223 (2022)

Yun, Y., Moon, S., Kim, S., Lee, J.: Flexible fabric-based GaAs thin-film solar cell for wearable energy harvesting applications. Sol. Energy Mater. Sol. Cells **246**, 111930 (2022)

Zhou, J., Huang, Q., Ding, Y., Hou, G., Zhao, Y.: Passivating contacts for high-efficiency silicon-based solar cells: from single-junction to tandem architecture. Nano Energy **92**, 106712 (2022)

Zhu, X., Su, H., Marcus, R.A., Michel-Beyerle, M.E.: Computed and experimental absorption spectra of the perovskite $CH_3NH_3PbI_3$. J. Phys. Chem. Lett. **5**(17), 3061–3065 (2014)

Authors and Affiliations

Khaled Gamal[1,2] · Mohammed Gamal[1,3] · Ali Okaz[2] · Nader Shehata[1,2,4,5,6] · Ishac Kandas[1,2]

✉ Khaled Gamal
kgamal@alexu.edu.eg

Mohammed Gamal
eng-mohammed.gamal.1520@alexu.edu.eg

Ali Okaz
ali.okaz@alexu.edu.eg

Nader Shehata
nader.shehata@alexu.edu.eg

Ishac Kandas
ishac.kandas@alexu.edu.eg

1   Center of Smart Materials, Nanotechnology, and Photonics (CSMPN), Smart Critical
    Infrastructure (SmartCI) Research Center, Alexandria University, Alexandria 21544, Egypt

2   Department of Engineering Mathematics and Physics, Faculty of Engineering, Alexandria
    University, Alexandria 21544, Egypt

3   Department of Electrical Engineering, Faculty of Engineering, Alexandria University,
    Alexandria 21544, Egypt

4   Kuwait College of Science and Technology, Doha Area, 7th Ring Road, 13133 Safat, Kuwait

5   USTAR Bio-Innovation Center, Utah State University, Logan, UT 84341, USA

6   School of Engineering, Ulster University, Belfast, Northern Ireland BT15 1AP, UK